
# A Microstructural and Kinetic Investigation of the KCl-Induced Corrosion of an FeCrAl Alloy at 600 A degrees C

Oxid Met (2015) 84:105–127
DOI 10.1007/s11085-015-9546-3

ORIGINAL PAPER

# A Microstructural and Kinetic Investigation of the KCl-Induced Corrosion of an FeCrAl Alloy at 600 °C

**N. Israelsson[1] · K. A. Unocic[2] · K. Hellström[1] · T. Jonsson[1] · M. Norell[3] · J.-E. Svensson[1] · L.-G. Johansson[1]**

Received: 2 February 2015 / Revised: 27 February 2015 / Published online: 18 March 2015


**Abstract** The corrosion behaviour of a FeCrAl alloy was investigated at 600 °C in $O_2 + H_2O$ with solid KCl applied. A kinetics and microstructural investigation showed that KCl accelerates corrosion and that potassium chromate formation depletes the protective scale in Cr, thus triggering the formation of a fast-growing iron-rich scale. Iron oxide was found to grow both inward and outward, on either side of the initial oxide. A chromia layer is formed with time underneath the iron oxide. It was found that although the alloy does not form a continuous pure alumina scale at the investigated temperature, aluminium is, however, always enriched at the oxide/alloy interface.

**Keywords** FeCrAl · High-temperature corrosion · Water vapour · KCl

## Introduction

In the last decade several countries have moved towards reducing their dependency on fossil fuels. As a result, renewable fuels such as biomass and waste are increasingly used for power production. Some European countries, e.g. Sweden, subsidises this type of environmentally friendly activities, thereby giving power plant owners an economic incentive to use this type of fuel. This means lower costs

✉ N. Israelsson
niklas.israelsson@chalmers.se

[1] The Swedish Competence Centre for High Temperature Corrosion, Chalmers University of Technology, 412 96 Göteborg, Sweden

[2] Materials Science & Technology Division, Oak Ridge National Laboratory, Oak Ridge, TN 37831, USA

[3] Department of Materials and Manufacturing Technology, Chalmers University of Technology, 412 96 Göteborg, Sweden

for carbon emissions and competitive fuel prices. Power boiler maintenance costs might, however, increase since biomass and waste contain more water and alkali chloride than traditional fuel [1–9]. Severe corrosion attacks have been recorded shortly after switching the fuel from coal to biomass/waste [10]. Super-heaters and water walls especially suffer from fireside corrosion. This corrosive environment leads to lower operating temperatures in order to increase the lifetime of the components in the boiler. In order to increase the energy output, higher operating temperatures are needed, which results in an increase in demands for new material that can cope with this aggressive environment.

Currently, low alloyed steels and stainless steels are the material of choice for use in these boilers. The ability of these alloys to withstand high temperatures relies on the formation of a protective, Cr-rich oxide $(Cr,Fe)_2O_3$. Previous studies have shown that certain chemical reactions consume the protective chromia scale and leave a poorly protective iron oxide behind [11–17]. This may result in a sudden increase in corrosion rate (breakaway corrosion). A possible strategy to avoid component failure in a power boiler would be to use a different type of material. One option would be to use an alumina-forming alloy such as the well-known FeCrAl. While FeCrAl alloys are known to form protective α-alumina scales when exposed to air and other oxygen-containing environments at 900 °C and higher [18], much less study has been devoted to the oxidation behaviour of FeCrAl alloys at lower temperatures. Investigating the oxidation behaviour of the FeCrAl alloy Kanthal® AF, [19, 20] Götlind et al. have reported that a protective alumina-rich scale formed in an oxidising environment at 600–900 °C. While no crystalline alumina was detected at 600 °C, α-alumina was reported to form at 700 °C and higher. In addition, Nicholls et al. [21] observed that a two-layered alumina scale formed after 1500 h oxidation at 800 °C with an outward growing transient alumina layer and an inward growing alumina layer which was interpreted as $\alpha$-$Al_2O_3$.

The influence of alkali chlorides and other chlorine-containing species on the high temperature corrosion of different metals/alloys has been investigated by several workers [15, 16, 22–26]. The strong acceleration of corrosion caused by HCl, KCl and NaCl has been attributed to alloy chlorination, e.g. by the "chlorine cycle" mechanism described by Grabke et al. [27] or more recently by an electrochemical mechanism [28–30]. Attention has also been directed towards the role of alkali in the breakdown of the protective chromia-rich scales on stainless steels. Thus, alkali chloride has been shown to react with the chromia in a scale under oxidizing conditions, forming alkali chromate (VI) according to Reaction (1):

$$1/2Cr_2O_3(s) + 2KCl(s) + 3/4O_2(g) + H_2O(g) \rightarrow K_2CrO_4(s) + 2HCl(g) \quad (1)$$

This process depletes the protective scale of chromium and tends to convert it to a poorly protective iron oxide scale, allowing alloy chlorination to proceed [31]. Because the reaction of KCl with $Al_2O_3$ to produce potassium aluminate ($KAlO_2$) is thermodynamically less favoured than $K_2CrO_4$ formation at the relevant temperature, it appears that alumina-forming alloys may provide a viable alternative for high temperature applications where materials are exposed to alkali chlorides under high $pO_2$ conditions at intermediate temperatures. However, little research has been

devoted to investigating the high temperature corrosion of FeCrAl alloys in the presence of alkali chlorides. Li et al. [32] have investigated the hot corrosion of Fe–Al, FeCrAl and FeCr alloys under a surface deposit of a NaCl-KCl melt at 670 °C. The study showed that the alumina-forming alloys coped relatively well with the aggressive environment, and that chromium played a detrimental role in the corrosion process. Li et al. [15] have also studied the effect of KCl vapour on Fe–Cr and FeCrAl alloys at 650 °C and reported that adding aluminium to the Fe–Cr alloy (with the same chromium content) increases the corrosion resistance of the alloy.

Recent papers report that a FeCrAl alloy forms potassium chromate in the presence of KCl in an $O_2 + H_2O$ environment at 600 °C according to Reaction (1), similar to FeCrNi alloys [12, 30, 33]. It was also reported that a alumina scale formed by pre-oxidation of a FeCrAl alloy (24 h, 700 °C) was somewhat resistant to attack by KCl [33]. The present study is a continuation of paper [33] where much of the corrosion behaviour was studied in the same environment as this investigation. In that paper, mass gain, X-ray Diffraction (XRD), Ion Chromatography (IC) and top-view Scanning Electron Microscopy with Energy Dispersive X-ray Spectroscopy (SEM/EDX) was used to describe the corrosion. The present study will further explore the microstructure of the cross-sections of the formed oxide scales with SEM/EDX, transmission electron microscopy with energy dispersive X-ray spectroscopy (TEM/EDX) and Auger Electron Spectroscopy (AES). In addition exposures were performed in a thermobalance to gain information about the in situ mass gain.

## Materials and Methods

The rapidly solidified powder based material Kanthal® APMT with the nominal composition given in Table 1 was exposed isothermally in a tube furnace in 5 % $O_2$ + 40 % $H_2O$ + 55 % $N_2$ at 600 °C for up to 168 h with a flow rate of 1000 ml/min, which corresponds to 3.2 cm/s. The samples with the dimensions 15 × 15 × 2 $mm^3$ (tube furnace) and 10 × 8 × 2 $mm^3$ (thermobalance) were ground with 320 grit SiC paper and polished in three steps using a 9, 3 and 1 μm diamond suspension. The polished coupons were degreased and cleaned using ultrasonic agitation in water, acetone and finally ethanol. A saturated solution of KCl in water/ethanol was used to add KCl to the sample surface prior to exposure. The specimen was alternately sprayed with the solution and dried with flowing air (∼35 °C) to avoid the formation of large droplets. The samples with 0.1 mg/$cm^2$ KCl were then allowed to stabilize in a desiccator before recording their weight with a six-decimal Sartorius balance. A Setaram TAG thermobalance was used to study the oxidation kinetics in the same type of environment as in the tube furnace

**Table 1** Nominal chemical composition of Kanthal® APMT, given in wt%

| Element | Fe | Cr | Al | Mo | Mn | Si | C | Reactive elements (RE) |
|---|---|---|---|---|---|---|---|---|
| wt% | Bal. | 21.0 | 5.0 | 3.0 | ≤0.4 | ≤0.7 | ≤0.08 | Y, Zr, Hf, Ta, Ti |

exposures. The flow rate was however, lower; 15 ml/min, which corresponds to 0.3 cm/s. The data were plotted from the time at which the isothermal exposure temperature was reached, which corresponded to 6 min. All analyses were performed on the samples exposed in the tube furnace.

A Siemens D5000 powder diffractometer was used to determine the crystalline corrosion products. The instrument was equipped with a grazing-incidence-beam attachment together with a Göbel mirror. The samples were exposed to a source of $CuK_\alpha$ radiation ($\lambda = 1.5418$ Å) with an incident angle of 0.5–1.5°. The moving detector collected data in the range of $20° < 2\theta < 65°$ with a step size of 0.05°. Silicon powder was added to the sample surfaces for calibration. The background was subtracted from the diffraction measurements.

Cross-sections with a width of roughly 500 μm were prepared using a Gatan Ilion$^+$ Broad Ion Beam (BIB) system. The ion gun was operated at 6 kV and the sputter time was 2–3 h. The cross-sections were analysed using SEM. An FEI Quanta 200 FEG ESEM operated in high vacuum mode was used in this study with an accelerating voltage of 3–25 kV. The instrument comes equipped with a Schottky Field Emission Gun (FEG) and an Oxford Inca EDX system, which was used for chemical quantification.

AES was conducted on one of the BIB cross-sections. The instrument used was a ThermoFisher Microlab 350 using an accelerating voltage of 10 kV and a beam current of about 1 nA, thus giving a nominal lateral resolution down to 12 nm. The area of interest was etched with 1 keV $Ar^+$ before the compositional analyse was performed in order to remove contaminants (carbon).

In order to obtain detailed microstructural information a Scanning Transmission Electron Microscope (STEM) was used. TEM characterization was carried out on a Philips model CM200 equipped with a Schottky Field Emission Electron gun (FEG) operated at an accelerating voltage of 200 kV and with an EDX from EDAX which was used for analytical analyses. Bright-field HR-STEM imaging and EDX mapping were obtained at 200 kV with a sub-Ångström probe on an aberration-corrected JEOL 2200FS-AC STEM using a CEOS $C_s$-Corrector equipped with a Bruker XFlash® 6|30 Silicon Drift Detector (SDD). STEM samples were prepared with a focus ion beam (FIB) in situ lift-out technique using a Hitachi NB5000 FIB-SEM and an FEI Strata DB 235M FIB-SEM.

## Results

### Initiation

Figure 1 shows plan view images of the alloy surface with the added KCl, before and after 10-, 30- and 60-min exposures in 5 % $O_2$ + 40 % $H_2O$ at 600 °C. The upper left image in Fig. 1 shows the distribution of KCl on the surface of the alloy before exposure, with salt crystallites ranging in size from a few to 100 μm. While the surface between the salt particles appears to be free from KCl, it has previously been found [29, 33] that small amounts of KCl are present in these areas. After only a 10-min exposure, numerous small particles (1–2 μm) identified as $K_2CrO_4$ using

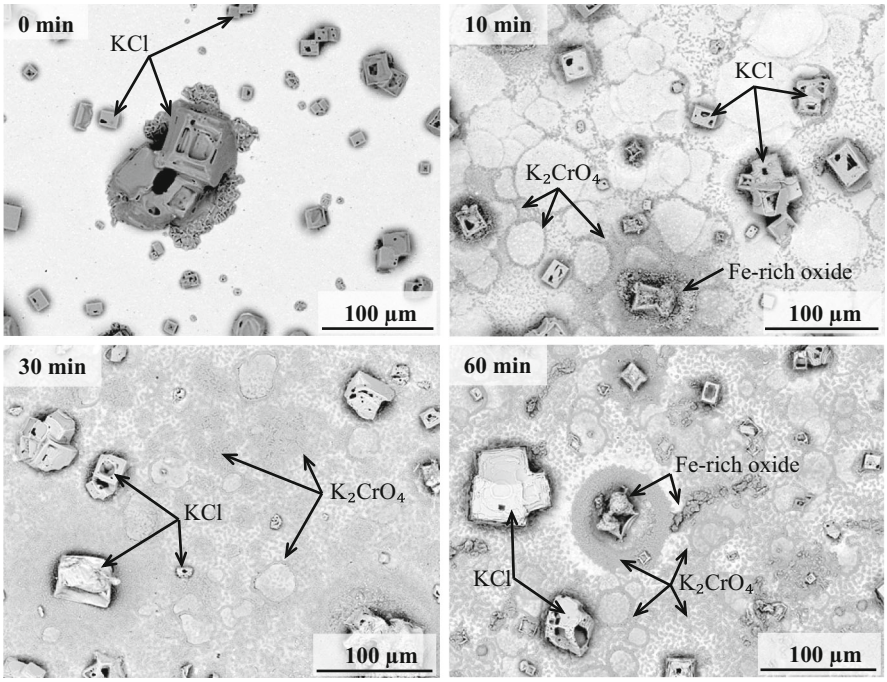


**Fig. 1** SEM-BSE top-view micrographs of Kanthal® APMT exposed with KCl for 0, 10, 30 and 60 min

XRD and SEM/EDX (not shown), had been formed on the surface. The $K_2CrO_4$ particles aggregated in a characteristic way forming circular patterns. It is suggested that this pattern reflects the initial distribution of KCl on the surface, which results from the spraying procedure (see experimental section). As early as this stage, some of the KCl crystals had been partly consumed and more or less overgrown by an iron-rich oxide that formed shell-like aggregates. After a 30-min exposure, more $K_2CrO_4$ particles had formed and the particle distribution had become more even than after the 10-min exposure. The sample exposed for 1 h showed the same features as seen after 10 and 30 min, and it appeared that chromate had continued to form in the time slot between 30 and 60 min. The top-view images in Fig. 3a, b are representative for most of the surface after 1 h, showing $K_2CrO_4$ particles on top of a smooth base oxide and a consumed salt crystal in the centre of the micrograph (Fig. 3a). There are a few areas on the surface where the smooth base oxide had detached from the alloy (Fig. 3c). EDX and XRD both show that unreacted KCl remained on the surface at this stage (Figs. 2, 3). For a comprehensive presentation of the XRD analysis, ex situ mass gains, ion chromatography analysis and SEM/EDX, see Israelsson et al. [33].

Figure 4 depicts a High Angle Annular Dark Field (HAADF)-STEM image of the cross-section of the corrosion product and the alloy substrate after one hour of exposure. The cross-section was obtained from an area represented by the boxed square in Fig. 3b. The image shows a thin (~400 nm), multi-layered oxide scale

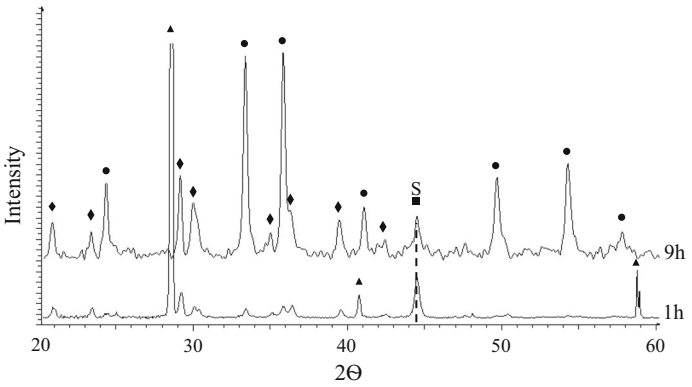


**Fig. 2** XRD diffractograms of Kanthal® APMT exposed for 1 and 9 h. The symbols indicate: $K_2CrO_4$ (*black diamond*), α-$(CrFe)_2O_3$ (*black circle*), KCl (*black up-pointing triangle*), and substrate (*black square*)

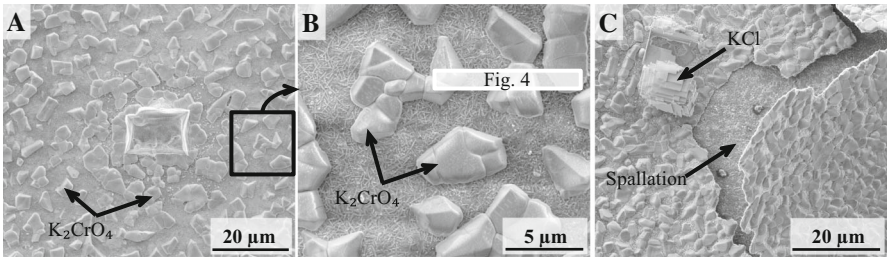


**Fig. 3** SEM-SE top-view micrographs of Kanthal® APMT after 1 h exposure. **b** shows an enlarged image of the boxed area in (**a**). The *boxed area* in (**b**) shows the area of the TEM foil shown in Fig. 4

with two $K_2CrO_4$ particles on top. The scale was partly cracked and a large void had formed in the middle. During the final sample thinning of the TEM foil, some of the scale at the bottom of the crack, to the left in the image, was milled away. Therefore, the STEM/EDX analysis was performed on the far right in the micrograph; the section that was least damaged by sample preparation. The STEM/EDX line profile from A to B in Fig. 4 shows mainly the chromium signal from the $K_2CrO_4$ particle. The relative weakness of the potassium signal is attributed to the decomposition of $K_2CrO_4$ in the electron beam. Potassium chromate decomposition during TEM analysis has been reported in earlier studies by Jonsson et al. [22]. The STEM/EDX point analyses (not shown) and the line scan from A to B in Fig. 4 reveals that the oxide scale beneath the $K_2CrO_4$ particle is layered. The bottom 1/5 contained high concentrations of Al and some Cr while the remaining part was dominated by Fe. The iron-rich top, 4/5 of the oxide, is suggested to contain the rhombohedral corundum-type solid solution $(FeCr)_2O_3$, identified using XRD (Fig. 2). The iron-rich part of the scale contained a rather narrow enrichment of chromium and aluminium, corresponding to the dark grey line seen in the STEM-

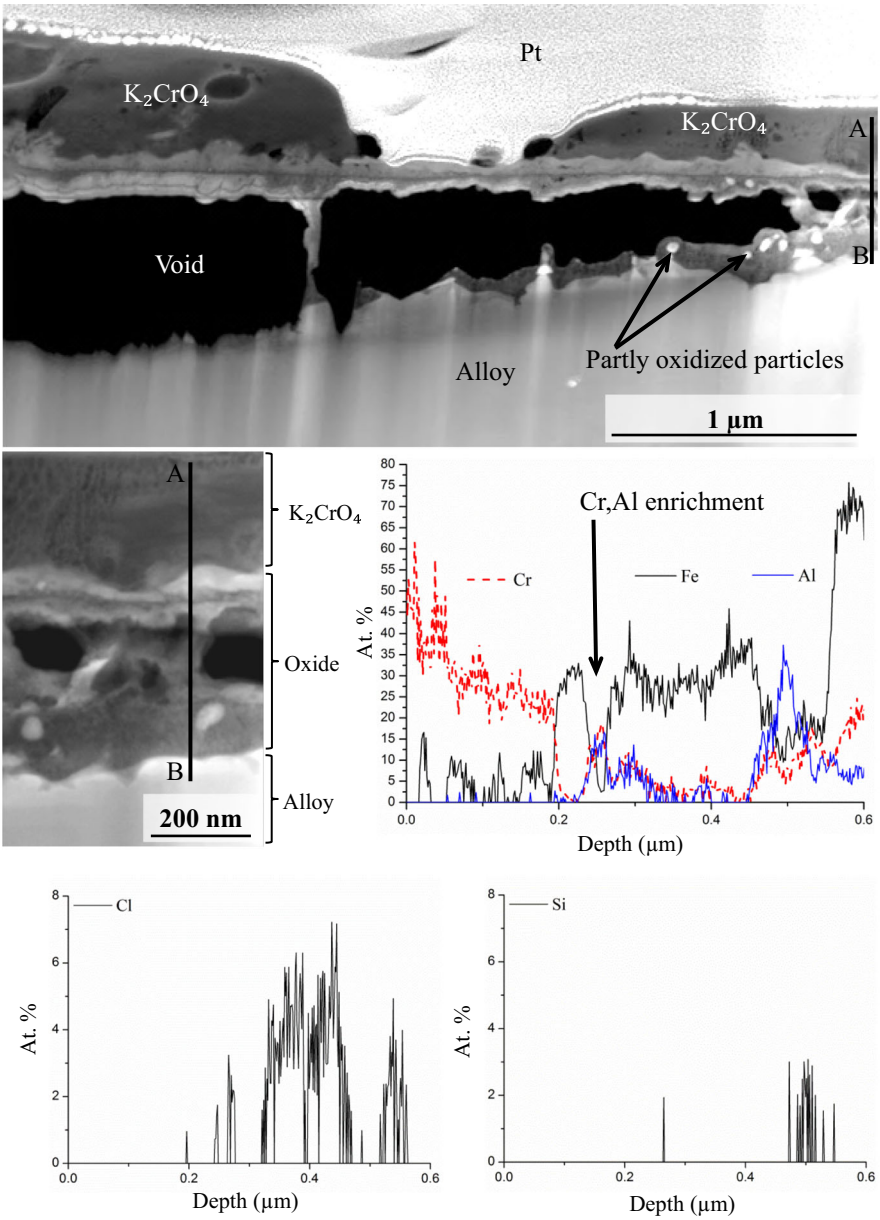


**Fig. 4** STEM-HAADF micrographs of the oxide scale formed after 1 h of exposure. The EDX line profile from *A* to *B* was obtained through the particle on top of the oxide scale as well as the oxide underneath (top micrograph). The second micrograph is an enlargement of the area where the line profile was obtained

HAADF image. This feature is suggested to correspond to the transient oxide formed in the initial stages of the exposure (see "Discussion" section). The top 50 nm of the oxide scale outside the (CrAl)-rich line was made up of almost pure

iron oxide. Chlorine was present in the scale beneath the (Cr, Al)-rich line, and formed discrete layers together with large amounts of Fe and some Cr. It is presumed that the Cl-rich regions correspond to mixtures of oxides and chlorides of Fe and Cr. Alumina-rich layers were sandwiched between the chlorine-rich regions. Also, chlorine enrichment occurred below the bottom Al rich scale layer, at the scale/alloy interface.

The STEM-HAADF image in Fig. 4 shows the partly oxidized particles (seen as bright spheres) which were dispersed in the oxide scale below the Cr–Al line. These particles were dominated by iron, molybdenum and silicon together with small amounts of chromium. It is suggested that oxygen is associated mainly with Si and Cr, while Fe and Mo are metallic. This type of particles becomes increasingly oxygen-rich when located closer to the oxide/gas interface. It may be noted that molybdenum was homogeneously dispersed in the as-received alloy.

**Breakaway/Propagation**

After 9 h, the added KCl had been entirely consumed (see Fig. 2 and Israelsson et al. [33]) and the KCl crystallites had been replaced by iron-rich oxide accumulations that formed shell-like structures resembling the shape of the original KCl crystallites. One such feature can be seen in the upper right corner of Fig. 5a (indicated by the arrow). Most of the sample surface can be described in terms of three typical morphologies (Fig. 5). One type of morphology is shown in Fig. 5b featuring $K_2CrO_4$ particles on the surface with a smooth base oxide between them, resembling the situation after 1 h (Fig. 3). The second type of morphology (Fig. 5c) shows characteristic features that are the remnants of former $K_2CrO_4$ particles and contain oxide whiskers. In the third type of morphology (Fig. 5d), the thin oxide has been replaced by a much thicker iron-rich scale with embedded $K_2CrO_4$ particles. The broad ion beam (BIB) cross-section in Fig. 5 is representative of the first and third morphology type described above. To the left in the image, there is a thin, smooth aluminium-rich scale with a $K_2CrO_4$ particle on top (compare Fig. 5b). To the right in the image, there is a much thicker, uneven layered scale (compare Fig. 5d). The top part of the thick scale consists of almost pure iron oxide and contains an embedded $K_2CrO_4$ particle. The dark line in the middle of the thick scale was enriched in aluminium and corresponds to the thin oxide scale to the left. The bottom part of the thick scale consisted of chromium-rich oxide which also contained considerable amounts of Al and Fe. The distribution of elements in the inner scale layer was difficult to analyse because of the relatively large lateral interaction volume of the electron beam ($\sim$0.5 μm). Below the scale, there was a $\sim$1 μm thick oxidation affected zone (OAZ) in the alloy with dark, needle-like particles. These particles are further analysed below.

The second type of surface morphology (a cross-section of decomposed $K_2CrO_4$ particles on top of a smooth oxide) is depicted in the STEM-HAADF image in Fig. 6 (from the boxed area in Fig. 5c). The main features were chromium oxide particles on top of a thin, alumina-rich scale with an OAZ below that contained aluminium-rich particles. The STEM/EDX mapping from the boxed area in Fig. 6 and the line profile (from A to B in Fig. 6) in Fig. 7 show that the particles on top of

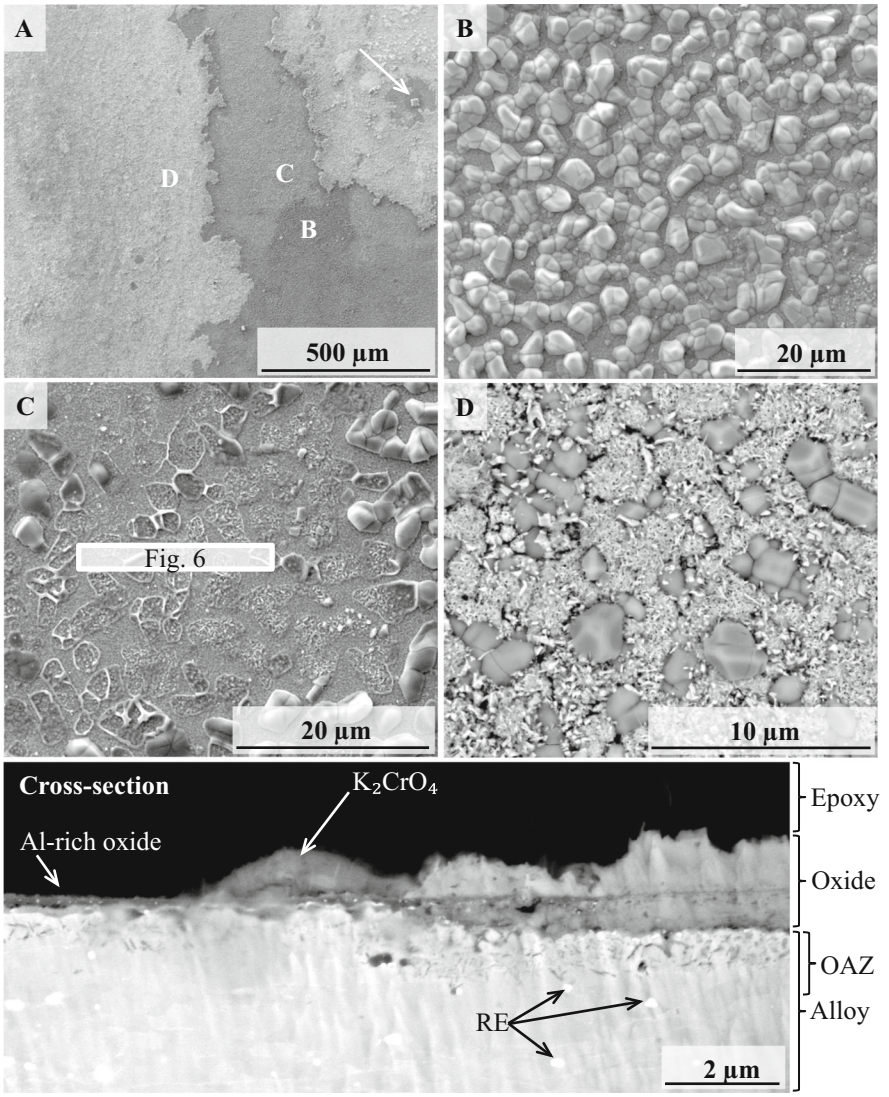


**Fig. 5** SEM-SE top-view micrographs (**a**–**c**) and SEM-BSE (**d** and BIB cross-section) of Kanthal® APMT exposed for 9 h. The *boxed area* in **c** shows the area of the TEM foil shown in Fig. 6

the thin oxide scale were dominated by chromium and oxygen with Cr making up 89 % of the cations according to STEM/EDX point analyses. In addition to Cr, the point analyses showed small amounts of Fe, Al, Mo and Cu, the copper signal originating from the TEM sample holder. Thus, it was concluded that these particles consist of $Cr_2O_3$. Figure 6 shows a 100–200 nm thick aluminium-rich oxide, similar to the thin oxide in the cross section in Fig. 5. The line profile in Fig. 7 shows that the oxide below the chromia particle was layered; the bottom part consisted of almost pure alumina while the outer part contained iron and chromium together with

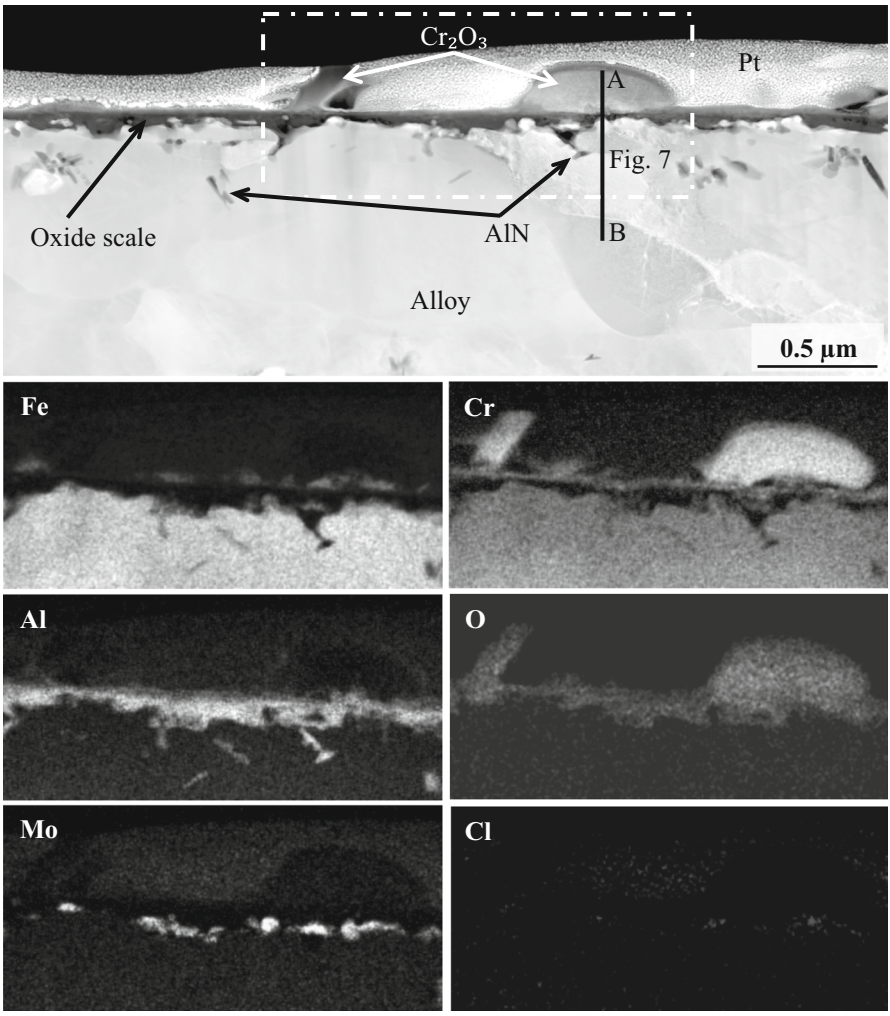


**Fig. 6** STEM-HAADF micrograph and EXD elemental maps of Kanthal® APMT exposed for 9 h. The TEM specimen was prepared from the boxed area in Fig. 5c

aluminium. Silicon was enriched at the alloy scale interface. Traces of chlorine were detected at the interface between the inner alumina layer and outer mixed FeCrAl oxide. STEM/EDX point analyses showed that the needle-like particles in the OAZ in Fig. 6 were enriched in aluminium and nitrogen suggesting that they consist of aluminium nitride. The molybdenum map in Fig. 6 shows that the Mo-rich partly oxidised metal particles seen after 1 h (Fig. 4) also were present after 9 h. The line scan in Fig. 7 reveals that the top 200 nm of the alloy below the scale was heavily depleted in aluminium and also depleted in Cr.

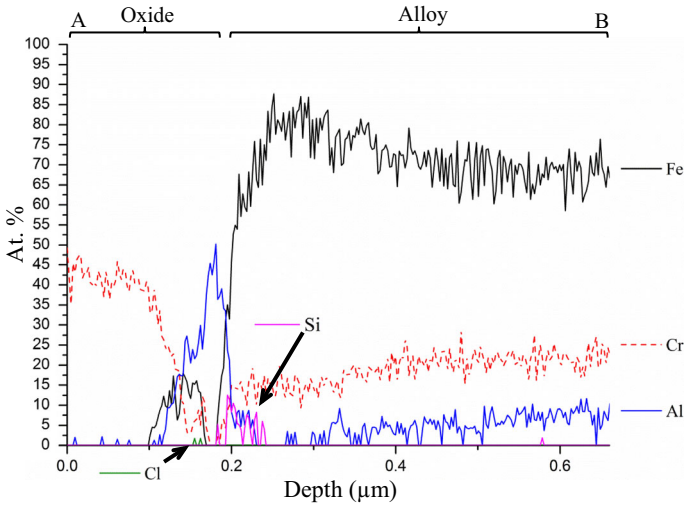


**Fig. 7** STEM/EDX line profile (from A to B in Fig. 6) through the remnant of the $K_2CrO_4$ particle and the oxide underneath

## Propagation

After 24 h of exposure, thick, iron-rich oxide of the type shown in Fig. 5d covered most (estimated 90–95 %) of the surface of the alloy (see Fig. 8). It was concluded in Israelsson et al. [33] that this iron-rich oxide corresponds to $\alpha$-$Fe_2O_3$ which was detected using XRD. Numerous $K_2CrO_4$ particles were still present at this stage.

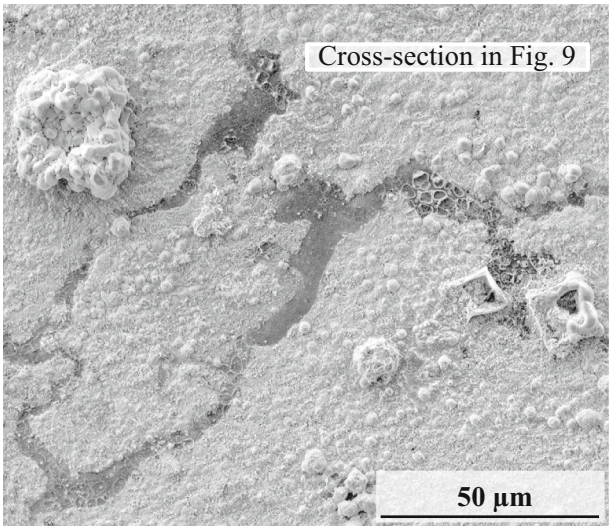


**Fig. 8** SEM-SE top-view micrograph after 24 h of exposure. The *boxed area* indicates the area of the obtained cross section in Fig. 9

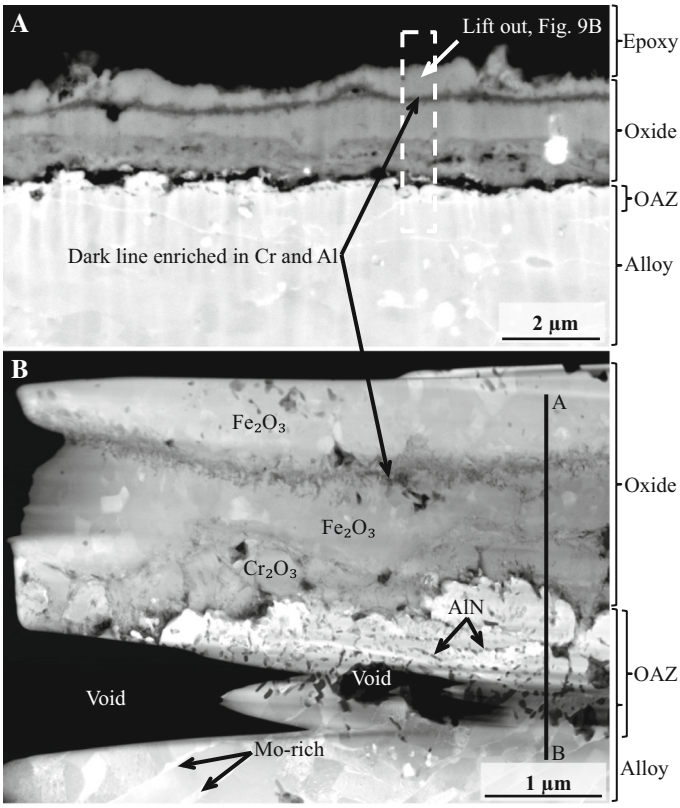


**Fig. 9** SEM-BSE micrograph of a one-sided cross-section (**a**) and a STEM-HAADF micrograph (**b**) of APMT exposed for 24 h. The TEM sample was prepared from the one-sided cross-section seen in the upper micrograph

According to ion chromatography (IC) analysis, the amount of chromate was about the same as after 9 h (see [33]). The parts of the surface not covered by thick iron-rich oxide had a morphology resembling that in Fig. 5c, which shows a smooth oxide with chromium oxide whiskers on top. The whiskers are presumably remnants of former $K_2CrO_4$ particles. After 24 h there was no sign of the surface morphology shown in Fig. 5b with $K_2CrO_4$ particles on top of a thin smooth oxide.

A ~500 µm long one-sided BIB cross-section was prepared from a part of the surface covered by thick iron-rich oxide. A representative part of the cross-section is shown in the upper SEM-BSE micrograph in Fig. 9a. This image reveals a layered oxide scale with a thickness of about 2 µm. According to the SEM/EDX analyses (not shown), the top 2/3 of the scale mainly consisted of iron oxide. A chromium-rich oxide layer was present beneath the iron-rich scale and an aluminium-enriched layer was present closest to the alloy. The latter corresponds to the 0.1–0.2 µm thick dark continuous line seen in Fig. 9a.

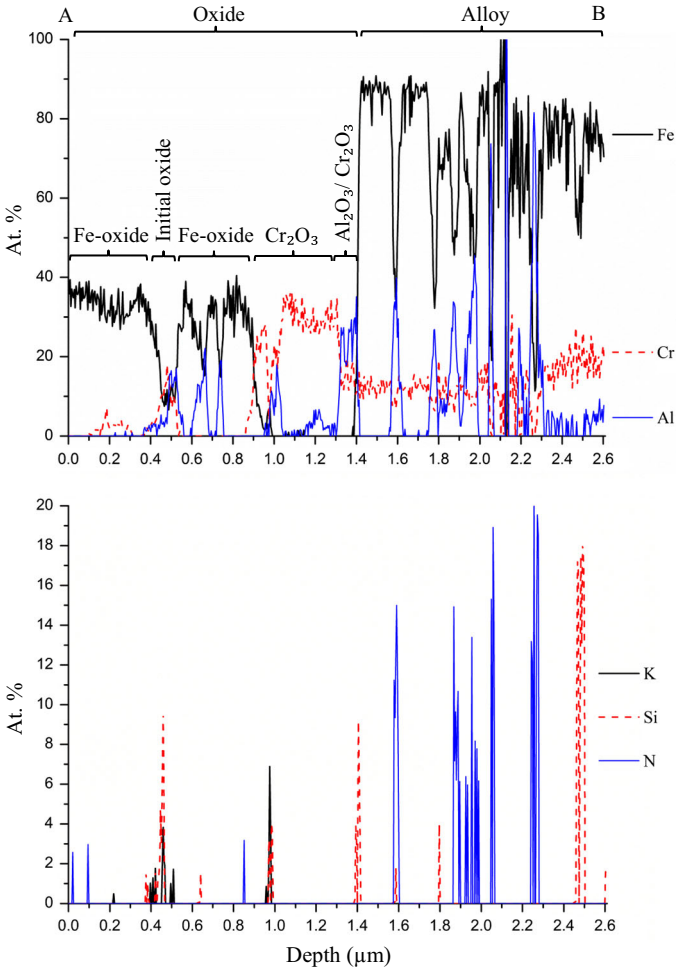


**Fig. 10** STEM/EDX line profile (from *A to B*) in Fig. 9 which reaches across the three layered oxide scale after 24 h of exposure

To provide detailed information about scale composition and to avoid problems with the (in this context) large interaction volume of SEM, a TEM sample was prepared from the boxed area in Fig. 9a. The thickness of the analysed slab was about 100 nm. Platinum was deposited to protect the sample during the preparation and thinning process. The STEM micrograph in Fig. 9b was complemented with the STEM/EDX line scan (from A to B in Fig. 9b) in Fig. 10 and with STEM/EDX point analyses.

The scale was seen to have a complex layered structure, the upper 2/3 of which were dominated by iron oxide. Fe corresponded to 98–99 % of the cations in several regions, according to the point analysis. In the middle of the iron oxide layer, there was an enrichment of Al and Cr together with some K and Si, corresponding to the

upper dark band in Fig. 9a, b. Below the iron oxide region, there was a chromium-rich oxide layer (Cr corresponded to 87 % of the cations, according to point analysis). This part of the scale was considered to be dominated by $Cr_2O_3$. At the interface between the iron oxide and chromia layer an Al enrichment occurred together with small amounts of Si and K (Fig. 10). At the scale/metal interface, there was a 0.1 μm thick layer which consisted of aluminium oxide together with considerable amounts of chromium oxide (Fig. 10). This region corresponded to the lower dark line in Fig. 9a. Silicon was enriched at the interface between scale and alloy (Fig. 10).

The transition from scale to metal corresponds to a sudden rise in Fe content in the line scan in Fig. 10. The top 0.5–1 μm of the alloy, immediately below the scale, was affected by oxidation and exhibited needle-like particles seen both in Fig. 9a, b. These particles were typically 20 by 100 nm in size (see Figs. 9, 11) being similar to

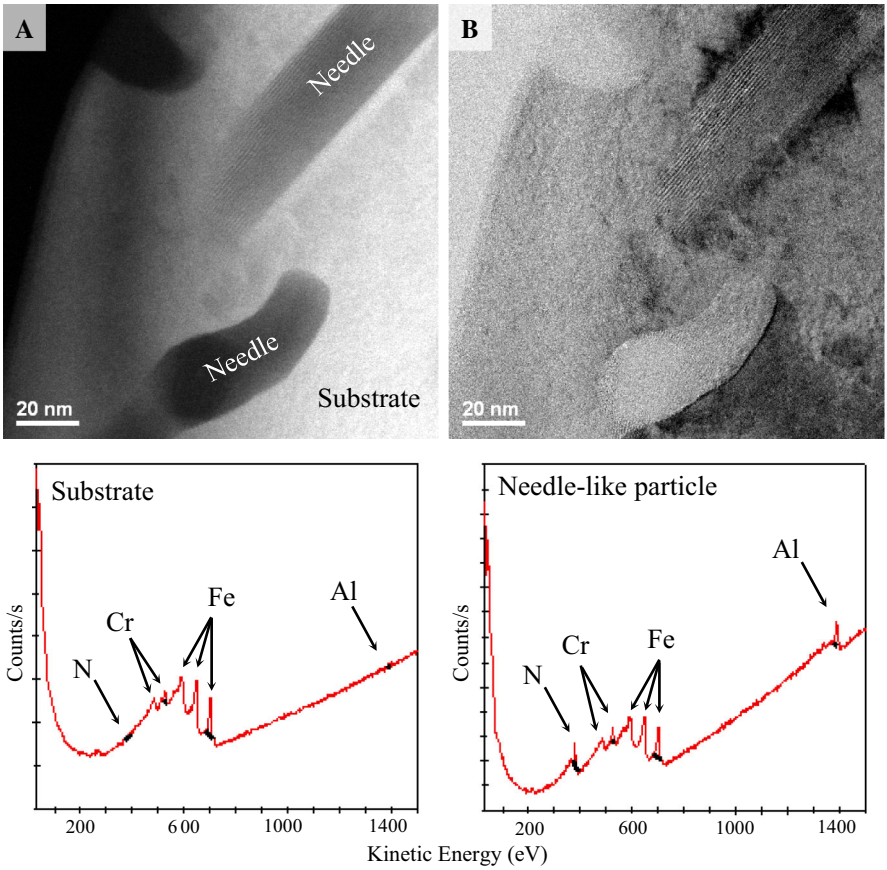


**Fig. 11** High resolution STEM-HAADF micrographs (**a**) and STEM-BF (**b**) of needle like particles after 24 h of exposure. Nano AES from the alloy substrate and a needle like particle is presented below the micrographs

those observed in the OAZ after 9 h (Fig. 6). The line scan in Fig. 10 shows that the particles were enriched in Al and N and it was concluded that they consisted of aluminium nitride (AlN). The amount of AlN as well as the depth of the OAZ increased from 9 to 24 h (compare Figs. 6, 9). As expected from the presence of AlN particles, the metallic constituent of the OAZ was strongly depleted of Al. The chromium level in the OAZ was about 12 at.%. Beneath the OAZ, the Al content increased and the Cr concentration rapidly reached its bulk value (~21 at.%) (Fig. 10).

Figure 9b shows bright lines in the alloy beneath the OAZ. Point analyses showed that the bright lines were enriched in Mo while the adjacent parts of the alloy contained no Mo, suggesting the presence of intermetallic Mo-rich precipitates.

The needle-like particles were subjected to AES on the nano-scale. Figure 11 shows two spectra, one from the alloy substrate next to a needle-like particle and the other from one of the particles. The AES analysis showed that the particle was enriched in Al and N. This is in accordance with the STEM/EDX line scan (see above) and point analyses, and supports the conclusion that the needle-like particles consist of AlN.

## Stagnation

Figure 12 shows a SEM-BSE micrograph of a one sided cross-section after 168 h at 600 °C. Similar to the situation after 24 h (compare Fig. 9a), Fig. 12 shows a layered scale on top of an OAZ in the alloy, the thickness of the oxide scale was in the range 1–2 μm. Analyses with SEM/EDX also showed that the layered structure was similar to the one described after 24 h with an iron oxide layer on top of a chromia layer and with an aluminium oxide rich zone at the scale/alloy interface. Two oxidized reactive element (RE)-rich particles were present in the oxide scale (Fig. 12).

Figure 12 shows that the OAZ contained two types of particles, i.e. small needle-like particles similar to those identified as AlN after 24 h and larger particles (with a dark contrast) that tended to align and form strings or layers in the upper part of the OAZ. The needle-like particles were larger and fewer in number after 168 h than

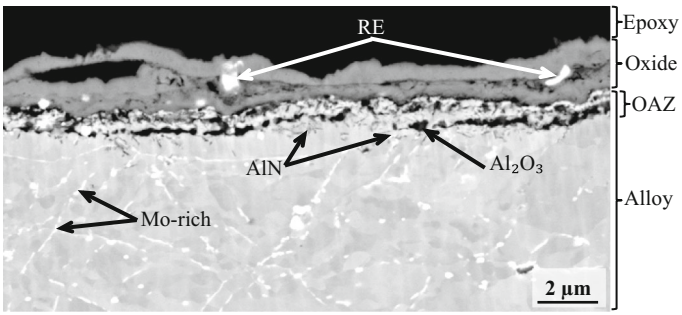


**Fig. 12** SEM-BSE micrograph of a one sided BIB cross-section of Kanthal® APMT exposed for 168 h

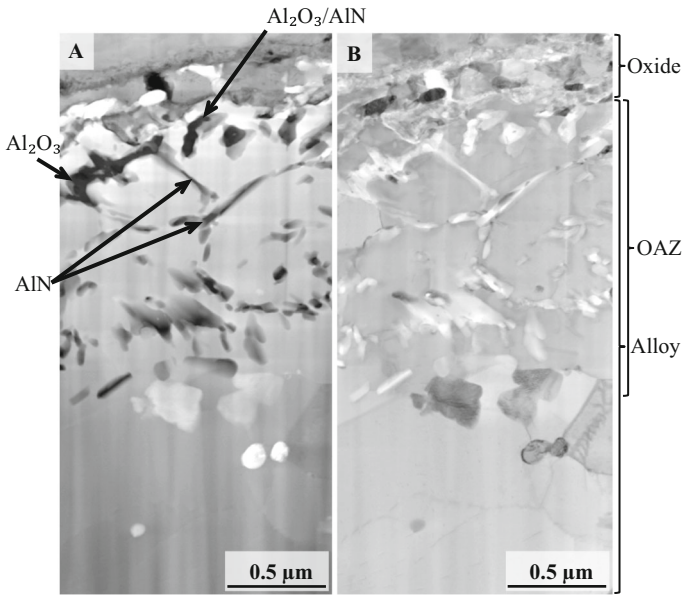


**Fig. 13** STEM-HAADF micrograph (**a**) and STEM-BF (**b**) of Kanthal® APMT exposed for 168 h

after 24 h, and extended 1.5–2 µm down into the alloy substrate. To analyse the OAZ in greater detail, a TEM specimen was prepared (Fig. 13). STEM/EDX point analyses confirmed that the needle-like particles consisted of AlN while the larger particles close to the scale interface were dominated by aluminium oxide. The STEM/EDX data show that some of these particles also contained nitrogen suggesting that they consisted of a mixture of $Al_2O_3$ and AlN (see Fig. 13). The elongated particles with a bright contrast at the interface between the oxide scale and the OAZ were partly oxidised metallic particles similar to the ones observed after 9 h.

## Gravimetry

Additional oxidation exposures were performed in a thermobalance in order to obtain information on oxidation kinetics. It may be noted that the exposure conditions in the thermobalance were slightly different from the tube furnace exposures, i.e., the average net flow velocity in the thermobalance was 0.3 cm/s compared to 3 cm/s in the tube furnace exposures. This difference may be significant as the rate of volatilization of, e.g. KCl and HCl from the surface depends on flow rate.

The mass gain curve in Fig. 14a has four distinct phases corresponding to initiation, breakaway, propagation and stagnation. When the sample was heated to 600 °C in the presence of KCl, mass gain was initially rapid and then slowed down somewhat between 1 and 5 h (initiation). Subsequently, mass gain accelerated for a few hours (breakaway) and then slowed down again (propagation), the mass gain

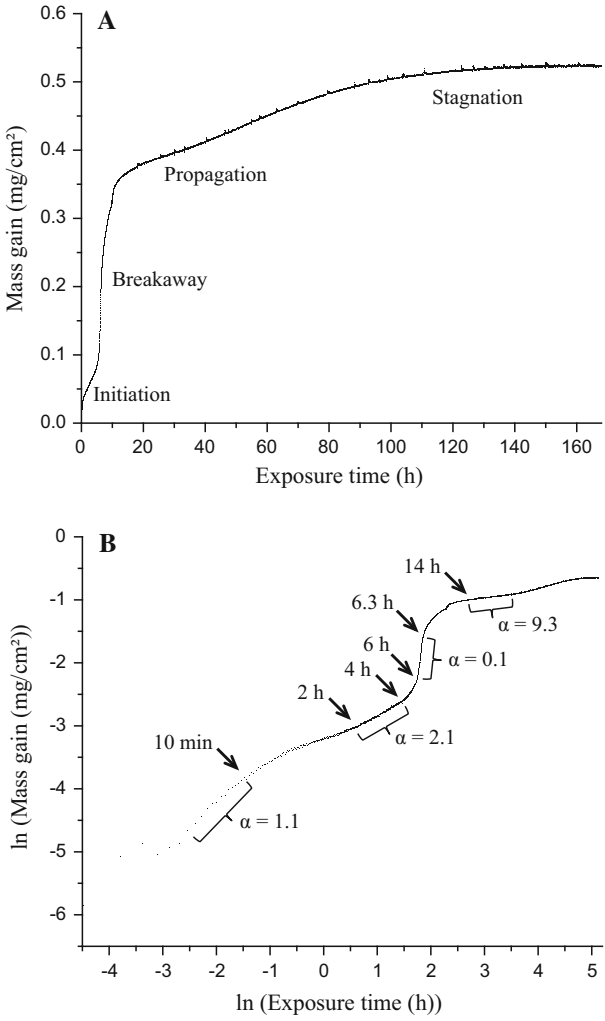


**Fig. 14** In-situ TGA (mass gain vs. exposure time) at 600 °C for up to 168 h (Fig. 14a). ln(mass gain)/ln(time) plot of in situ TGA (mass gain vs. exposure time) in (Fig. 14b)

curve became almost flat after 100 h (stagnation). It should be noted that several exposures were performed in the thermobalance in order to validate the shape of the mass gain curve in Fig. 14a. Figure 14b shows an ln(mass gain) versus ln(time) plot of the data in Fig. 14a. The slope of the ln(mass gain) versus ln(time) plot corresponds to $1/\alpha$ where $\alpha$ is the exponent in the kinetic expression:

$$m^{\alpha} \propto t \tag{2}$$

Thus, a constant (linear) mass gain corresponds to $\alpha = 1$ while parabolic growth corresponds to $\alpha = 2$.

The plot in Fig. 14b displays several linear sections with characteristic slopes. Initially there was a short period during which $\alpha$ was $\sim 1$, corresponding to a linear mass gain. Then came a stage where $\alpha$ was about 2, corresponding to the initiation phase with the slower mass gain (1–5 h) in Fig. 14a. The breakaway phase in Fig. 14a corresponded to a decrease in the value of $\alpha$ to 0.1. Subsequently, the value of $\alpha$ increased with exposure time reaching about 9 after 14 h.

## Discussion

The present results show that Reaction (1) is rapid at 600 °C since large amounts of $K_2CrO_4$ are detected after only 10 min (Fig. 1). The initially somewhat uneven occurrence of potassium chromate on the surface of the alloy is attributed to the distribution of KCl before exposure (Fig. 1). Chromate formation is connected to the initiation phase in Fig. 14a where no thick, iron-rich oxide can be observed on the top surface (see Fig. 3b). Because of the rapid reaction and the limited amount of KCl available, the reaction that forms chromate is essentially completed after 9 h; XRD (Fig. 2) and SEM/EDX showing no evidence for KCl at this stage. This is also supported by the previous quantitative analysis of the kinetics of Reaction (1) on the same alloy [33]. Consequently, the chlorination of the alloy by KCl has ceased after 9 h.

It was suggested in [30, 33] that $K_2CrO_4$ decomposes with time and forms $Cr_2O_3$. The present results confirm that potassium chromate particles do form chromia whiskers (Figs. 5c, 6). $K_2CrO_4$ decomposition is suggested to proceed by means of the following electrochemical reaction:

$$K_2CrO_4(s) + H_2O(g) + 3e^- \rightarrow 1/2Cr_2O_3(s) + 2KOH(l) + 3/2O^{2-}$$

$$Cr(alloy) \rightarrow Cr^{3+} + 3e^-$$

$$\Sigma: \; K_2CrO_4(s) + H_2O(g) + Cr(alloy) \rightarrow Cr_2O_3(s) + 2KOH(l) \qquad (3)$$

$\Delta G^\circ_{873K} = -231.4$ kJ, [34] corresponding to a standard cell potential E° of +0.80 V.

The amount of chromate formed on the surface of the alloy is substantial, corresponding to the amount of chromium in a 0.45 μm thick layer of the alloy, considering that all added KCl reacted according to Reaction (1). The observation of metal chlorides in the cross-section after 1 h (Fig. 4) shows that only part of the chlorine added as KCl was lost in the form of HCl(g), according to Reaction (1). Several researchers have reported that high temperature alloys can be chlorinated in $O_2$-containing gases with HCl(g) [35, 36]. However, chlorination with HCl(g) is not considered to be the main source of sub-scale chloride in the present case. This is because the flowing gas will dilute the HCl generated by Reaction (1) and transport it away from the sample. Instead it is suggested that the transition metal chlorides are formed directly from KCl, by means of an electrochemical reaction:

$$2KCl + 5/4O_2 + 1/2Cr_2O_3(s) + 2e^- \rightarrow K_2CrO_4(s) + 2Cl^-$$
(at the scale surface)

$$Fe(alloy) \rightarrow Fe^{2+} + 2e^-$$

$$\Sigma: \ 2KCl(s) + 5/4O_2(g) + 1/2Cr_2O_3(s) + Fe(alloy) \rightarrow K_2CrO_4(s) + FeCl_2(s) \quad (4)$$

$\Delta G^{\circ}_{873K} = -141.458$ kJ, [34] corresponding to a standard cell potential E° of +0.73 V.

While Reactions (1) and (4) both contribute to the formation of chromate, it is suggested that the main source of chromate in the present case is Reaction (1), because it is favoured by the high concentration of water vapour (40 vol%). Obviously, Reaction (1) cannot play any role under dry conditions. While Grabke et al.,[27] suggested that alkali chloride can react with $Cr_2O_3$ and $O_2$ to form alkali chromate (VI) and gaseous chlorine, that reaction is not thermodynamically favoured in the present case, and is, thus, disregarded. It was reported by Israelsson et al. [30] that when exposed to KCl at 600 °C, an FeCrAl alloy will form much more transition metal chloride in dry $O_2$ than in an $O_2 + H_2O$ environment. It is suggested that this is due to the consumption of most of the KCl by Reaction (1) in the $O_2 + H_2O$ environment. The poor adherence between the iron-rich oxide layer and the inner alumina-rich layer in Fig. 4 is believed to be connected to the presence of transition metal chloride at this interface. The observation that transition metal chlorides become scarce after 24 h and are absent after 168 h is attributed to hydrolysis and volatilization and to the fact that all added KCl has been consumed at this stage.

Figure 3c shows a case where the initial oxide scale, which is covered by an almost continuous $K_2CrO_4$ layer, has detached from the alloy. It is suggested that the spallation has been caused by the presence of metal chlorides at the scale metal interface and the large mismatch in thermal expansion coefficients between scale and alloy. Thus, while the thermal expansion coefficient of the alloy is about $13.6 \times 10^{-6}$/K and $7.3 \times 10^{-6}$/K for $Cr_2O_3$, [37], the corresponding value for $K_2CrO_4$ is much higher at about $50 \times 10^{-6}$/K [38]. It is argued that spallation occurred during cooling when the exposure was discontinued. There were no signs of spallation after longer exposure times.

Upon exposure to high temperature, an alloy initially forms a thin (about 0.1 μm) alumina-rich oxide (see Figs. 5, 6), which is then replaced by a thicker, layered scale where the initial oxide is sandwiched between outward- and inward-growing layers of iron oxide. The initial oxide is seen to the left in the cross-section image in Fig. 5, and the iron oxide/alumina/iron oxide sandwich is seen to the right in the same image, the Al-rich part forms a dark grey band. The same oxide layer sequence is also present in Figs. 4 and 9. The breakaway behaviour illustrated in Fig. 14a is attributed to the formation of the fast growing iron-rich oxide shown in Fig. 5d and on the right hand side of the cross section image in Fig. 5. The STEM/EDX line profiles show that the top oxide layer essentially consists of iron oxide, corresponding to hematite (Figs. 4, 10). It is concluded that this layer was formed

by the outward diffusion of iron ions. The inward-growing iron oxide layer (situated immediately beneath the initial oxide) is more complex and also contains small amounts of chromia, alumina and, after short exposure times, transition metal chlorides (Fig. 4). As noted above, the reaction of all added KCl to form potassium chromate would require an amount of chromium corresponding to a $\sim$0.45 μm thick layer of the alloy. The oxidation of such a depleted zone (assuming that it consists of iron) corresponds to the formation of a 0.8 μm thick layer of $Fe_2O_3$. This correlates fairly well with the combined thickness of the duplex iron oxide, not counting the sandwiched alumina-rich oxide. Young et al. [39] have extrapolated diffusivity data for binary Fe–Cr alloys to 600 °C from estimates by Whittle et al. [40] for the temperature range 900–1200 °C. Based on that data and using a $D_{Cr}$ of $10^{-14.5}$ $cm^2/s$, the diffusion length of chromium in the alloy after 24 h could be calculated to be only 0.17 μm. This implies that alloy oxidation/chlorination and chromate formation occur concurrently, as the oxidation front advances. After 24 h (Fig. 9) when all the KCl had been consumed, there appears a layer of relatively pure chromia (about 87 % of the cations) appeared at the bottom of the scale. At the scale/alloy interface, the Cr oxide layer had been enriched in alumina (see Fig. 10). This is in marked contrast to corresponding exposures of Fe–Cr–Ni alloys in the same environment. In that case it was reported that the breakdown of the protective scale in the presence of KCl and $O_2 + H_2O$ resulted in a scale consisting of an FeCr spinel oxide at the bottom with an iron oxide top part [41]. It is suggested that this difference may be due to a lower oxygen activity at the oxide/alloy interface due to the aluminium content of the alloy.

Figures 4 and 10 show that the scales contain several alumina-rich layers and that the oxide at the scale/alloy interface is always enriched in alumina. Two such layers were detected after 1 h while there were at least five alumina layers within the scale after 24 h (Fig. 10). It is assumed that these layers represent a succession of events during which the aluminium in the alloy has been preferentially oxidized. Consequently, the alumina-rich layer found at the scale/alloy interface would be the most recent one. An inspection of Fig. 10 shows that while some alumina-rich layers contain chromium, the two alumina-rich layers that are immersed in the inward-grown iron oxide do not. It is suggested that the latter (chromia-free) alumina layers correspond to the internal oxidation of an alloy that has been depleted of chromium due to potassium chromate formation (see above). The situation is not as clear-cut after 1 h, perhaps because the alloy was not fully Cr depleted at this early stage (Fig. 4).

The mass gain during the propagation stage (see Fig. 14a) is partly attributed to the spreading of the thick scale over the entire surface and partly to the continued slow growth of the thick scale. The penetration of chlorine beneath the initial protective oxide after 1 h (Fig. 4) leads to the conclusion that KCl has caused it to fail, partly through Reaction (1) which depletes the oxide scale and the alloy substrate in chromium, and partly through chlorination of the alloy (Reaction 4). It may be noted that chlorine had also penetrated the bottom alumina/chromia-rich layer at this stage (Fig. 4), and it is suggested that this will cause this protective oxide layer to fail with time. The exhaustion of the KCl supply on the surface of the alloy and the resulting cessation of $K_2CrO_4$ formation and alloy chlorination are

suggested to explain the slow rate of oxidation after long exposure times during the stagnation phase (Fig. 14a). After long exposure times when corrosive species are absent, the oxidation rate will mainly depend on the protective properties of the chromia/alumina layer at the bottom of the scale.

Oxidation usually dominates high temperature corrosion reactions in the presence of $O_2$ and other oxygen donors such as $H_2O$ and $CO_2$. However, when $N_2$ is present, and if the oxide scale is not protective, alloys are known to suffer from internal nitridation along with oxidation. Alloys that contain strong nitride formers, e.g. Al and Ti, are especially susceptible to nitride formation [42]. The literature reports on the formation of AlN in e.g., Fe–Al, Ni–Cr–Al, Cr–Al and FeCrAl alloys at high temperatures [43–45]. However, the literature on AlN formation in FeCrAl alloys is scarce. In a recent paper by Pint et al. [45] it was reported that un-doped ferritic Fe(Al) + Cr model alloys formed AlN in air at 700–1000 °C, the amount of nitrides increasing with temperature. In contrast, nitridation was not observed in the corresponding alloys when reactive elements were added to the alloys. Bennet et al. [43] have reported on AlN formation on the commercial FeCrAl alloy PM2000 at 1200 °C in a simulated crevice/crack in an $N_2$ environment at low $PO_2$. It was argued that the oxygen potential in the gas penetrating into the crevice/crack decreased due to the formation of oxide, which allowed nitridation to occur.

AlN formation was not detected when the investigated material was exposed to $O_2 + H_2O + N_2$ in the absence of KCl [33]. In the present case, AlN was observed after exposure times exceeding 1 h. While the amount of nitride and the penetration depth increased between 9 and 24 h, the nitridation of the alloy appeared not to have progressed further after 168 h. Instead, it appeared that AlN was converted to alumina at this stage. Because the $N_2$ molecule is quite stable and only dissociates with difficulty on oxide surfaces at this temperature, alloy nitridation implies that the oxide scale is permeable to $N_2$ molecules. Interestingly, it appears that this was the case not only for the thick-layered oxide formed after breakaway, but also for the initial alumina-rich oxide (Figs. 5, 6). It is argued that the rapid corrosion attack connected to $K_2CrO_4$ formation and alloy chlorination (Reactions 1, 4) creates pathways for $N_2$ molecules to penetrate through the oxide scale. For example, the decomposition and volatilization of the transition metal chlorides formed early during the corrosion process (Fig. 4), are expected to produce porosity in the scale. The $N_2$ molecules that penetrate the scale subsequently dissociate at the metal surface and dissolve into the alloy. The present results show that nitridation interferes with the oxidation behaviour of the alloy. Thus, as a result of the Al depletion of the alloy due to AlN precipitation (Fig. 10) the alloy is unable to re-form an external alumina scale. It was observed that the AlN particles coarsen with time and slowly transform into $Al_2O_3$ after long exposure times (Figs. 12, 13). The transformation is suggested to occur according to Reaction (5):

$$3/2O(ss) + AlN(s) \rightarrow 1/2Al_2O_3(s) + N(ss) \quad (5)$$

It is suggested that the nitrogen released into the matrix in this way diffuses deeper into the alloy where the Al activity is higher, thus forming new AlN particles. This is supported by the observation that the AlN particles were detected

at a greater distance from the scale/alloy interface after 168 h (approximately 1.5–2 μm) than after 24 h (approximately 1 μm); see Figs. 9, 12 and 13.

## Conclusions

- KCl strongly accelerated the corrosion of Kanthal® APMT in an $O_2 + H_2O$ environment at 600 °C. Chromia in the scale reacted rapidly, forming $K_2CrO_4$ and gaseous HCl.
- Chromate formation depleted the protective scale in Cr, triggering the formation of a fast-growing iron-rich scale. Iron oxide grew both inward and outward, on either side of the initial oxide. With time, a chromia layer formed underneath the iron oxide and an aluminium enrichment was always present closest to the alloy surface.
- $K_2CrO_4$ was reduced on the scale surface by an electrochemical process in which the electrons are supplied by means of alloy oxidation.
- Transition metal chlorides formed after short exposure times. The chlorinating agent is suggested to be KCl, which reacts electrochemically.
- The formation of AlN caused aluminium depletion of the alloy and reduced its ability to form a protective alumina scale.

**Acknowledgments** The Microscopy Research was supported by the Center for Nanophase Materials Sciences (CNMS), which is sponsored by the Scientific User Facilities Division, Office of Basic Energy Sciences, U.S. Department of Energy. The authors would like to thank D.W. Coffey for assistance with TEM sample preparations.



## References

1. H. P. Michelsen, F. Frandsen, K. Dam-Johansen and O. H. Larsen, *Fuel Processing Technology* **54**, 95 (1998).
2. B. Sander, *Biomass and Bioenergy* **12**, 177 (1997).
3. L. L. Baxter, T. R. Miles, T. R. Miles Jr., B. M. Jenkins, T. Milne, D. Dayton, R. W. Bryers and L. L. Oden, *Fuel Processing Technology* **54**, 47 (1998).
4. R. L. Bain, R. P. Overend and K. R. Craig, *Fuel Processing Technology* **54**, 1 (1998).
5. B. M. Jenkins, L. L. Baxter, T. R. Miles Jr and T. R. Miles, *Fuel Processing Technology* **54**, 17 (1998).
6. H. Kassman, J. Pettersson, B.-M. Steenari and L.-E. Åmand, *Fuel Processing Technology* **105**, 170 (2013).
7. P. Viklund, A. Hjörnhede, P. Henderson, A. Stålenheim and R. Pettersson, *Fuel Processing Technology* **105**, 106 (2013).
8. M. Montgomery and A. Karlsson, *Materials and Corrosion* **50**, 579 (1999).

9. F. Frandsen, H. Nielsen, P. Jensen, L. Hansen, H. Livbjerg, K. Dam-Johansen, P. B. Hansen, K. Andersen, H. Sørensen, O. Larsen, B. Sander, N. Henriksen and P. Simonsen, *Deposition and Corrosion in Straw- and Coal-Straw Co-Fired Utility Boilers*, (Springer, Berlin, 1999).
10. H. H. Krause, Corrosion/93, NACE International **200** (1993).
11. H. Asteman, J.-E. Svensson, M. Norell and L.-G. Johansson, *Oxidation of Metals* **54**, 11 (2000).
12. C. Pettersson, L.-G. Johansson and J.-E. Svensson, *Oxidation of metals* **70**, 241 (2008).
13. S. Karlsson, J. Pettersson, L.-G. Johansson and J.-E. Svensson, *Oxidation of Metals* **78**, 83 (2012).
14. M. Halvarsson, J. E. Tang, H. Asteman, J.-E. Svensson and L.-G. Johansson, *Corrosion Science* **48**, 2014 (2006).
15. Y. S. Li, Y. Niu and M. Spiegel, *Corrosion Science* **49**, 1799 (2007).
16. Y. S. Li, M. Sanchez-Pasten and M. Spiegel, *Materials Science Forum* **461–464**, 1047 (2004).
17. F. Liu, J. E. Tang, T. Jonsson, S. Canovic, K. Segerdahl, J.-E. Svensson and M. Halvarsson, *Oxidation of Metals* **66**, 295 (2006).
18. J. Engkvist, S. Canovic, K. Hellström, A. Järdnäs, J.-E. Svensson, L.-G. Johansson, M. Olsson and M. Halvarsson, *Oxidation of Metals* **73**, 233 (2010).
19. H. Josefsson, F. Liu, J.-E. Svensson, M. Halvarsson and L.-G. Johansson, *Materials and Corrosion* **56**, 801 (2005).
20. H. Götlind, F. Liu, J.-E. Svensson, M. Halvarsson and L.-G. Johansson, *Oxidation of Metals* **67**, 251 (2007).
21. J. R. Nicholls, M. J. Bennett and R. Newton, *Materials at High Temperatures* **20**, 429 (2003).
22. T. Jonsson, J. Froitzheim, J. Pettersson, J.-E. Svensson, L.-G. Johansson and M. Halvarsson, *Oxidation of Metals* **72**, 213 (2009).
23. J. Lehmusto, P. Yrjas, B. J. Skrifvars and M. Hupa, *Fuel Processing Technology* **104**, 253 (2012).
24. S. Enestam, D. Bankiewicz, J. Tuiremo, K. Mäkelä and M. Hupa, *Fuel* **104**, 294 (2013).
25. C. Pettersson, J. Pettersson, H. Asteman, J.-E. Svensson and L.-G. Johansson, *Corrosion Science* **48**, 1368 (2006).
26. M. A. Uusitalo, P. M. J. Vuoristo and T. A. Mäntylä, *Corrosion Science* **46**, 1311 (2004).
27. H. J. Grabke, E. Reese and M. Spiegel, *Corrosion Science* **37**, 1023 (1995).
28. N. Folkeson, L.-G. Johansson and J.-E. Svensson, *Journal of the Electrochemical Society* **154**, C515 (2007).
29. T. Jonsson, N. Folkeson, J.-E. Svensson, L.-G. Johansson and M. Halvarsson, *Corrosion Science* **53**, 2233 (2011).
30. N. Israelsson, K. Hellström, J. E. Svensson and L. G. Johansson, *Oxidation of Metals* **83**, 1 (2015).
31. J. Pettersson, N. Folkeson, L.-G. Johansson and J.-E. Svensson, *Oxidation of Metals* **76**, 93 (2011).
32. Y. S. Li, M. Spiegel and S. Shimada, *Materials Chemistry and Physics* **93**, 217 (2005).
33. N. Israelsson, J. Engkvist, K. Hellström, M. Halvarsson, J. E. Svensson and L. G. Johansson, *Oxidation of Metals* **83**, 29 (2015).
34. C. W. Bale, E. Bélisle, P. Chartrand, S. A. Decterov, G. Eriksson, K. Hack, I. H. Jung, Y. B. Kang, J. Melançon, D. Pelton, C. Robelin and S. Petersen, *Calphad* **33**, 295 (2009).
35. P. Viklund and R. Pettersson, *Oxidation of Metals* **76**, 111 (2011).
36. H. P. Nielsen, F. J. Frandsen, K. Dam-Johansen and L. L. Baxter, *Progress in Energy and Combustion Science* **26**, 283 (2000).
37. P. Kofstad, *High Temperature Corrosion*, (Elsevier Applied Science Publishers Ltd., London, 1988).
38. C. W. F. T. Pistonius, *Zeitschrift für Physikalische Chemie* **35**, 109 (1962).
39. D. J. Young, J. Zurek, L. Singheiser and W. J. Quadakkers, *Corrosion Science* **53**, 2131 (2011).
40. D. P. Whittle, G. C. Wood, D. J. Evans and D. B. Scully, *Acta Metallurgica* **15**, 1747 (1967).
41. C. Pettersson, J. Pettersson, H. Asteman, J.-E. Svensson and L.-G. Johansson, *Corrosion Science* **48**, 1368 (2005).
42. G. Lai, *High Temperature Corrosion and Materials Application*, (ASM International, Materials Park, 2007).
43. M. J. Bennett, J. R. Nicholls, G. Borchardt and G. Strehl, *Materials at High Temperatures* **19**, 117 (2002).
44. S. Han and D. J. Young, *Oxidation of Metals* **55**, 223 (2001).
45. B. A. Pint, M. J. Dwyer and R. M. Deacon, *Oxidation of Metals* **69**, 211 (2008).